How do deep-water volcanoes grow?

Qiliang Sun[1,2,3], Craig Magee[4], Christopher A-L. Jackson[5], Samuel J. Mitchell[6], Xinong Xie[1,3]

[1]Key Laboratory of Tectonics and Petroleum Resources, China University of Geosciences (Wuhan), Ministry of Education, Wuhan 430074, China;

[2]Laboratory for Marine Mineral Resources, Qingdao National Laboratory for Marine Science and Technology, Qingdao 266061, China;

[3]College of Marine Science and Technology, China University of Geosciences (Wuhan), Wuhan, Hubei 430074, PR China;

[4]Institute of Geophysics and Tectonics, School of Earth and Environment, University of Leeds, Leeds, LS2 9JT, UK;

[5]Basins Research Group (BRG), Department of Earth Science & Engineering, Imperial College, London, SW7 2BP, UK;

[6]Department of Earth Sciences, University of Bristol, Bristol, BS8 1RJ, UK

Abstract

Deep-water volcanoes are emplaced in water depths >1.0 km and are widespread along continental margins and in ocean basins. Whilst the external morphology of deep-water volcanoes can be mapped using bathymetric surveys, their internal structure and true volume remain enigmatic. It is thus difficult to determine how deep-water volcanoes grow. We investigate 13

Late Miocene-to-Quaternary, deep-water volcanoes that are imaged in 3D by seismic reflection data from the northern South China Sea, which allow us to quantify their external morphology and examine their internal structure. These deep-water volcanoes were emplaced in water depths >1.5 km, are relatively small (<3.0 km diameter, <0.56 km tall, and <0.92 km^3 in volume), and have steep slopes (up to 42º). Most of the volcanoes have erosional, 'crater-like' bases, infilled with sub-horizontal seismic reflections. These crater-like bases are overlain by downward-converging, conical seismic reflections delineating the classical volcano morphology. We suggest the crater-like bases formed by excavation of cold, wet, and poorly consolidated near-seabed sediment during expulsion of hydrothermal fluid, and not by explosive magmatic eruptions or gravitational subsidence. Erupted igneous material infilled the precursor craters with the observed sub-horizontal layers, likely comprising hyaloclastites. After this initial phase of volcanism, the buildup of volcanic material produced layers that are now represented by the flank-parallel or downward-converging, conical seismic reflections. We suggest high hydrostatic pressures of >15 MPa, which are typical of water depths >1.5 km, inhibited degassing and fragmentation of ascending magma and thus erupted lava. This lack of degassing and fragmentation permitted effusive eruptions during the latter stages of volcanism. Our models for volcano growth in the deep submarine realm demonstrate the power of using 3D seismic data when investigating the internal structure and total volume of deep-water volcanoes.

Keywords: deep-water volcanoes, volcanism, extrusion dynamics, growth mechanism, erosion, South China Sea

1. Introduction

Volcanoes occur in a variety of plate boundary and intra-plate settings across Earth's surface. Determining how volcanoes grow is not only critical to predicting and mitigating volcanic hazards, but this understanding can also provide information on the underlying plumbing system structure (e.g., feeder and reservoir locations) and magma dynamics (e.g., composition and supply rate) (e.g., Moore and Clague, 1992; Arnulf et al., 2014; Clague et al., 2018). Volcanoes emplaced on land are typically well-studied and, by comparing their external morphology to similar neighboring edifices, we can infer they are broadly built through fluctuations between so-called summit- and diameter-prone growth (e.g., Moore and Clague, 1992; Rossi, 1996; Grosse et al., 2009; Karlstrom et al., 2018). Yet without direct access to volcano interiors, it is difficult to test growth models predicted from their external morphology alone. Examining ancient, (partially) eroded volcanoes provides some insight into how volcanoes are constructed, but modification of their original shape means we cannot assess relationship between internal structure and external morphology (e.g., Goto and Tomiya, 2019). By using traditional remote-sensing and/or field-based techniques, we can therefore either quantify the external morphology of uneroded volcanoes, but not know their internal structure, or study the interiors of eroded volcanoes where information on their original edifice shape has been lost. Our ability to only constrain either the external morphology *or* internal structure of onshore volcanoes, but not both, limits our understanding of how volcanoes grow.

Remote sensing data and lithostratigraphic analysis of well cores allow us to constrain the external geometry and internal structure of the evolution of shallow- and deep-water volcanoes (e.g., Smith, 1988; Magee et al., 2013; Cocchi et al., 2016; Buchs et al. 2018). In particular, seismic reflection imaging of volcanoes provides a unique opportunity to resolve uncertainties regarding volcano growth, given these data can image both the external morphology *and* internal structure of volcanoes (e.g., Gatliff et al., 1984; Calves et al., 2011; Magee et al., 2013; Reynolds et al., 2018; Sun et al., 2019). For example, by using 2D seismic reflection data offshore southern Australia, Magee et al. (2013) showed trends in the external morphology of buried, shallow-water shield volcanoes were consistent with growth via summit eruptions and a proportionate increase in summit height and volcano diameters. Interpretation of reflections within the volcanoes reveal the majority of volcanoes did indeed grow by a proportionate increase in summit height and basal diameter (i.e. the layers were parallel to the volcano flanks) (Magee et al., 2013; see also Reynolds et al., 2018). A similar seismic-based study of shallow-water volcanoes (water depth <200 m), emplaced along the western Indian rifted margin, reveal they preferentially grew via increases in diameter without a commensurate increase in summit height (Calves et al., 2011). Whilst seismic reflection data have been used to unravel the growth of shallow-water volcanoes, few studies have utilized these data to study the internal structure of deep-water (>1 km) volcanoes (e.g., Gatliff et al., 1984; Sun et al., 2019). We note a recent scientific expedition collected seismic reflection data imaging the Axial Seamount, a volcano formed along the Juan de Fuca Ridge in water depths of 1.4-2.8 km (Arnulf et al., 2014).

Discerning how deep-water volcanoes erupt and grow is critical for: (1) accurate assessment of deep-water volcanic hazards (e.g. submarine landslides and associated tsunami; e.g. Staudigel and Clague, 2010); (2) calculation of accurate eruptive and total volume estimates, which contribute to understanding melting conditions in the underlying crust and/or mantle (e.g. Buchs et al., 2018; Sun et al. 2019); and (3) determining the role of volcanoes in gas venting and hydrothermal circulation (e.g. Planke et al., 2005). Importantly, high hydrostatic pressures in deep-water settings, which can inhibit degassing, ascent rate, and fragmentation of magma, mean the extrusion dynamics of deep-water volcanoes may fundamentally differ from their onshore and shallow-water counterparts (e.g. Gregg and Fornari, 1998; Cas and Simmons, 2018; Carey et al., 2018; Manga et al., 2018; Sun et al., 2019). These differences in eruption style and underlying controls suggest we may not be able to simply apply our knowledge of volcanism in other, subaerial or shallow water settings, to understand how deep-water volcanoes grow (e.g. Gregg and Fornari, 1998; Manga et al., 2018). It is therefore necessary to image the internal structure of deep-water volcanoes to reveal their growth history.

Here, we use 3D seismic reflection data to investigate 13 deep-water volcanoes located along the continental margin of the northern South China Sea. These Late Miocene-Present volcanoes were emplaced close to the Continent-Ocean Boundary (COB) in water depths >1.5 km. Our 3D seismic reflection data allow us to map the external morphologies and internal structures of these volcanoes in unprecedented detail. From our seismic reflection imaging, we propose the majority of studied deep-water volcanoes grew through an initial phase of crater formation driven by escape of hydrothermal fluids, which became infilled. Volcanic cones developed on top of these infilled craters, or in two cases directly on undisturbed seabed sediment, primarily grew by proportionate increases in summit height and basal diameter, thereby maintaining their slope angle; some volcanoes appear to have grown by preferential addition of material to summit regions. Although similar growth models have been proposed for volcanic cones in subaerial and shallow marine settings, we demonstrate the deep-water volcanoes we study are relatively smaller and have steeper slopes. We attribute the initial phase of crater formation and morphological differences between deep-water volcanoes and those in other settings, to the unique physical conditions under which deep-water volcanoes evolve. Our work shows seismic reflection data is a powerful tool for unravelling volcano growth.

2. Geological setting

The South China Sea is located in a complex tectonic region between the Eurasian, Pacific and India-Australia plates (e.g. Briais et al., 1993; Franke et al., 2014; Li et al., 2014) (Fig. 1a). The South China Sea evolved as a magma-poor rift, culminating in seafloor spreading, the onset of which varied across the region (e.g. Clift et al., 2001; Cullen et al., 2010; Larsen et al., 2018). Seafloor spreading began in the East Sub-basin in the early Oligocene (~33 Ma; Briais et al., 1993; Li et al., 2014), before the spreading center jumped to the Southwest Sub-basin in the late Oligocene (~25 Ma) (e.g. Franke et al., 2014). Spreading ceased sometime in the middle Miocene (~15.0-15.5 Ma; Briais et al., 1993; Li et al., 2014). Since the late Miocene (~10.5 Ma), tectonic activity in the northeastern part of South China Sea has been mainly driven by its collision with the Philippine Sea Plate (i.e. the Dongsha Event; e.g. Lüdmann and Wong, 1999).

The study area is located to the south of Dongsha Islands in the northern South China Sea (Fig. 1a). Geological and geophysical studies (e.g. borehole, gravity, magnetic, and 2D and 3D seismic reflection data) indicate widespread Cenozoic volcanism across the northern South China Sea (e.g. Li and Liang, 1994; Yan et al., 2006; Zhao et al., 2016). From the early Paleocene to earliest Oligocene, before the onset of seafloor spreading, intermediate-acidic volcanoes were emplaced in a subaerial setting (Yan et al., 2006). From the Oligocene to middle Miocene, there was a compositional and environmental transition to the emplacement of mafic-to-intermediate volcanoes in shallow-water (<200 m) and subaerial settings (e.g. Yan et al., 2006; Lester et al., 2014) (Fig. 1a). Rapid post-emplacement subsidence led to these volcanoes being deeply buried (up to depths of 1.5 km) beneath the current seafloor (e.g. Zhao et al., 2016). Late Miocene and younger, intra-plate volcanoes (Figs. 1b-c) were emplaced close to the continent-ocean boundary (Clift et al., 2001; Sun et al., 2019). Recent IODP Expeditions 349/367/368 drilled several of these deep-water volcanoes in the South China Sea, revealing they are primarily basaltic (e.g. Li et al., 2014; Larsen et al., 2018), and that some were emplaced during continental breakup and directly covered by deep-water (>1.3 km) nanofossil-bearing clay sediments (Larsen et al., 2018). Many of the deep-water volcanoes, emplaced since the Late Miocene, feed long run-out lava flows that have irregular basal morphologies (Sun et al., 2019) (Figs. 1b-c). The volumes of these long run-out lavas appear equivalent to, or substantially greater than, that of the erupted material contained in the volcanoes themselves (Sun et al., 2019).

3. Datasets and methods

We use a time-migrated 3D seismic reflection dataset covering ~1150 km^2 to study the external morphology and internal structure of deep-water volcanoes in the South China Sea (Fig. 1a). The data were acquired in 2012 using eight tuned air source guns, each with a volume of 8×20 in^3, to produce a total shot volume of 8×160 in^3. Six 3000 m-long, 240-channel streamers with a spacing of 12.5 m were used to tow the hydrophones. The data are zero-phase processed with ordinary processing procedures (e.g. digital filtering, deconvolution, dynamic/static correction, offset stack, etc.), and displayed with Society of Exploration Geophysicists (SEG) normal polarity. A downward increase in acoustic impedance therefore corresponds to a positive reflection event (red on displayed seismic profiles) and a downward decrease in acoustic impedance corresponds to a negative reflection (black on displayed seismic profiles) (e.g. Brown, 2004).

The dominant frequency in the interval of interest (i.e. 0–400 m below the seabed) is ~40 Hz. The estimated limit of separability within the deep-water strata (i.e. nanofossil-bearing clay) encasing the volcanoes is ~14 m, based on a seismic velocity of 2.2 km/s for the sedimentary rocks; this velocity is derived from nearby seismic refraction profiles (Yan et al., 2001; Wei et al., 2011) (Fig. 1a). There are no seismic velocity data available for the studied deep-water volcanoes, but we assume they have an interval velocity of the 4.0±1.0 km/s based on: (i) measured seismic velocities of ~3.0-5.0 km/s for basaltic rocks (lava flows, volcaniclastic breccias and pyroclastics) intersected by nearby boreholes (e.g. BY7-1 and IODP 1431) (Li et al., 2014; Zhao et al., 2016); (ii) velocities of ~3.0-5.5 km/s obtained from seismic refraction profiles that cover other deep-water volcanoes within the basin (Yan et al., 2001; Wei et al., 2011); (iii) typical seismic velocities calculated from boreholes penetrating basaltic submarine volcanoes (~3.3-5.5 km/s) elsewhere (Calvès et al., 2011); and (iv) the size of observed seismic velocity anomaly-induced 'pull-ups' beneath the studied volcanoes (V7, V11, and V13, Fig. S1), caused by acoustic waves travelling faster through hard, crystalline igneous rocks than the surrounding sedimentary strata (Jackson, 2012; Magee et al., 2013; Reynolds et al., 2018). With regard to the latter point, we calculate interval velocities of 3.2-4.1 km/s for the three volcanoes (V7, V11, and V13), derived from the magnitude of velocity pull-up artifacts (~82.7 ms - 161.3 ms TWT high) present in underlying seismic reflections (Fig. S1):

$$\mathrm{Vpi} = \frac{Ts \times Vps}{Ti}$$

where Vps (Vps = 2.2 km/s) and Vpi are the seismic velocities of encasing rocks/sediments and igneous rocks; Ts and Ti are the seismic wave travel time in the encasing rocks/sediments and igneous rocks, respectively (Fig. 2a).

Given a dominant frequency of ~40 Hz and an interval velocity of the 4.0±1.0 km/s, the estimated limits of separability and visibility of layers within the volcanoes is 19-31 m (λ/4) and 3-4 m (λ/30), respectively (Sun et al., 2019). When the volcanic structures are thicker than the estimated limit of separability, their top and base reflections can be distinguished. However, if their thickness lies between the limits of separability and visibility, they will appear as tuned reflection packages; i.e. reflections from their top and base interfere on their return to the surface and cannot be distinguished (e.g. Brown, 2004). Volcanic structures thinner than the limit of visibility will likely not be distinguishable from noise within the seismic data (Eide et al., 2017).

The volcanoes we study comprise two distinct components, involving a volcanic edifice and an underlying infilled crater-like base (Fig. 2b). We mapped three key seismic horizons: TV (top of volcano), BV (base of volcano), and the seabed (Figs. 3a-c). From these mapped horizons, we measured key geomorphologic parameters of the volcanoes, including diameter and height/depth of the edifices and crater-like bases (Fig. 2b). We define volcano thickness, which we also use to calculate volume, as the difference in height between TV and BV (Fig. 2b); volume estimates also take into account the irregular morphologies of TV and BV. Because the observed volcano flanks are rugged, we calculated average flank dips as height/(diameter/2) (Fig. 2b). In places, where volcanoes appear to merge, we constrain the plan-view extent of each edifice by distinguishing the location of minimum thickness between them (Fig. 3d). Errors in height, depth, volume, and flank dip measurements largely arise from uncertainties in the seismic velocities (4.0±1.0 km/s) used to undertake the depth conversion rather than measurement errors. The collected edifice and crater dimensions data will allow us to better understand how much volcanic material may essentially be underestimated from other geophysical techniques, and thus unaccounted for when calculating volumes of magma production. We compare the geomorphologic characteristics of the volcanic edifices to volcanoes emplaced in different environments with varying composition, such as ocean basins (Basalt; Smith, 1988), subaerial volcanic arcs (Basalt - andesite; Grosse et al., 2009), submarine volcanic arcs (dacite, basalt-andesite; Wright et al., 2006) and shallow water (Basalt; Magee et al., 2013).

4. Characteristics of the deep-water volcanoes

4.1. Seismic expression

We mapped the top and bases, and thus constrained the thickness and volume of 13 volcanoes (Figs. 3b-c; Table 1). In our seismic data, several volcanoes appear to have merged to form a single, large edifice defined by multiple distinct summits (i.e. V4-V6 and V11-V12; Figs. 3b-c). All the volcanoes are at least partly buried by a thin layer (<300 m) of Late Miocene- Quaternary strata (Figs. 4-5; Table 1), with the tips of edifices (i.e. V6, V7, V9, V11, V12 and V13) breaching the seabed (Figs. 3a, 4a-b, 4d, 4f). Except for V1, all volcanoes are encircled by moats that are up to 75 m deep, and which, depending on their stratigraphic occurrence, are unfilled (i.e. moats expressed at seabed), partly infilled, or fully filled (i.e. buried moats) (e.g. V6-V9; Figs. 3a, 4a-b, 4d-f, 5). The volcanoes are typically characterized by continuous-to-moderately continuous, high-amplitude top reflections (i.e. TV), and discontinuous, primarily low-amplitude base reflections (i.e. BV) (Figs. 4-5; Fig. S1). Occasionally BV is continuous and high-amplitude (e.g. V6; Fig. 4f). Projected boundaries dividing the crater-like bases and edifices of individual volcanoes occur at different stratigraphic levels (Fig. 4). For example, the edifice-crater boundary for V12 is coincident with the modern seabed, whilst for V9 the edifice-crater boundary is located ~50–100 ms TWT (~40-80 m) beneath the current seafloor (Figs 4a-b).

We identify two types of volcano bases: (i) crater-like bases that truncate underlying seismic reflections (Figs. 4a-d); and (ii) relatively flat bases that are conformable with underlying strata (e.g. V6 and V8; Figs. 4e-f). Based on these differences in basal geometry, we sub-divide the volcanoes into two groups: (i) GP1 (11 volcanoes), which have crater-like bases (Figs. 4a-d); and (ii) GP2 (2 volcanoes), which have strata-concordant bases (Figs. 4e-f). The bases of both groups of volcanoes are located at various stratigraphic horizons, up to ~264 m beneath the seabed. Seismic reflections directly beneath the volcanoes, as well as those below lavas emanating from the volcanic edifices, have very low-amplitude compared to their typical seismic character away from the overlying volcanoes (Fig. 5). These reflections beneath the volcanoes are also typically disturbed and occasionally appear to be deflected upward relative to their regional dip (e.g. those beneath V9 in Fig. 5).

4.2. External volcano morphology and dimensions

4.2.1. Volcano edifices

The volcanic edifices have circular to elliptical basal sections, with diameters of ~0.6–3.0 km (average of ~1.3 km), covering areas of ~0.25-7.15 km^2 (Table 1). Edifice height ranges from ~79±20 to 560±140 m (Figs. 3b, 6a; Table 1). There is a very weak (i.e. R^2 = ~0.21), positive correlation between edifice diameter and height, with an average height:diameter ratio of 0.25 (Fig. 6a). Flanks are linear, convex-upward, or convex-downward, and are moderate-to-steep, with dips of up to 42º (average dip of ~26º) (Figs. 4-5; Figs. S1-S2); most (nine) of the volcanoes have slopes >20º (Table 1). Flank dip is weakly, negatively correlated with edifice diameter (R^2 = ~0.12; Fig. 6b) and weakly, positively correlated with height (R^2 = ~0.39; Fig. 6c). Overall, edifice volumes range from ~0.0160±0.0040 to 0.9213±0.2303 km^3 and show a strong, positive correlation to diameter (R^2 = ~0.94; Fig. 6d), but a weak correlation to height (R^2 = ~0.25; Fig. 6e) and no correlation with flank dip and volume (R^2 = ~0.06) (Fig. 6f).

4.2.2. Crater-like bases

The depth and diameter ranges of the crater-like bases are ~87±22 to 517±129 m and ~0.8 to 4.6 km, respectively, and only weakly, positively correlated (R^2 = ~0.20) (Fig. 7a; Table 1); their volumes range from 0.0082±0.0021 to 0.8144±0.2036 km^3 (Table 1). The dips (5º-32º) of the basal crater flanks are only weakly, negatively correlated to crater diameter (R^2 = ~0.29; Fig. 7b) and very weakly, negatively correlated with depth (R^2 = ~0.17; Fig. 7c). Crater volume is moderately-to-strongly, positively correlated (R^2 = ~0.65) with crater diameter but only weakly correlated to crater depth (R^2 = ~0.22) and very weakly, negatively correlated with crater flank dip (R^2 = ~0.16) (Figs. 7d-f).

4.2.3. Total volcano morphometrics

The heights of volcano edifices and depths of crater-like bases are weakly, positively correlated (R^2 = ~0.36; Fig. 7g), whilst their diameters are moderately-to-strongly, positively correlated (R^2 = ~0.65; Fig. 7h). We note the diameters of the crater-like bases are typically greater than (e.g. V5 and V11) or equal to (e.g. V10 and V13) those of their overlying edifices (Fig. 7h). These differences in diameter mean that the *volumes* of crater-like bases are typically larger than those of the overlying edifices (Fig. 7i), e.g. by more than five times (e.g. V5; Table 1); the volumes of the crater-like bases and edifices are weakly, positively correlated (R^2 = ~0.23; Fig. 7i).

The average diameters, combining that of the edifices and crater-like bases, of individual volcanoes show a weak (R^2 = ~0.22), positive correlation to volcano thickness (Fig. 7j). The total volumes of volcanoes range from 0.0277±0.0070 to 1.2669±0.3167 km^3. Volcano thickness is only weakly (R^2 = ~0.28) positively correlated with total volcano volume (Fig. 7k). However, there is a strong (R^2 = ~0.88), positive correlation between total volcano volume and average diameter (Fig. 7j).

4.3. Internal architecture and seismic facies

We define two principal intra-volcano seismic facies (Fig. 4). Seismic facies 1 (SF1) is bound at its base by BV and predominantly comprises discontinuous, short, parallel to sub-parallel, moderate- to high-amplitude seismic reflections within the crater-like bases of GP1 (Figs. 4a-d). Reflections within SF1 appear broadly parallel with those of the surrounding sedimentary layers. Some outwardly dipping seismic reflections, which define broadly conical structures, are locally observed within the cores of SF1 (Figs. 4a-d). Overlying SF1, seismic facies 2 (SF2) constitutes the upper parts of all GP1 and GP2 volcanoes, broadly comprising stacked, continuous-to-moderately continuous, moderate-amplitude reflections that downlap onto SF1 or BV (Fig. 4). In most instances the internal SF2 reflections, where clearly observed, broadly parallel the outer margins of the volcanic edifices (e.g. Figs 4a, e-f); in some edifices the SF2 reflections converge down-dip (e.g. Fig. 4b).

5. Discussion

5.1 Age and environment of volcanism

Biostratigraphic data from nearby boreholes constrain the age of the nanofossil-bearing sedimentary sequences encasing the 13 mapped volcanoes, which have edifice bases that mark the syn-eruptive seabed located at different stratigraphic levels (Figs. 4-5), and indicate volcanism occurred periodically between the Late Miocene (e.g. ~6.3 Ma of V1; Sun et al., 2019) and Quaternary. Analysis of ODP (Site 1146) and IODP (Site U1501) data reveal that, at least since the Early Miocene (~23 Ma) and throughout this prolonged period of intermittent volcanism, the study area was a deep-water (>1.0 km) environment (e.g. Clift et al., 2001; Li et al., 2014; Larsen et al., 2018). Because the mapped volcanoes are within an area characterized by a present water depth of >1.3 km, and the Miocene-Quaternary sea level was ~200 m higher (Xu et al., 1995), it is likely volcano emplacement occurred in water depths >1.5 km; these water depths correspond to overlying hydrostatic pressures of >15 MPa.

5.2. Volcano formation and growth

Most of the thirteen mapped volcanoes (11 of 13) can be sub-divided into an edifice and a crater-like base developed (Figs. 4a-d, 5). These crater-like bases truncate the underlying stratigraphic reflections and are infilled by sub-horizontal reflections, onto which a conical edifice is developed (Figs. 4a-d, 5). Here we discuss how each of these features relates to the initiation and growth of these deep-water volcanoes.

5.2.1. Formation of crater-like bases

Crater-like bases have been observed beneath volcanoes and hydrothermal vents in subaerial and shallow-water settings, and their formation has primarily been attributed to disaggregation and material removal during explosive eruptions (e.g. Planke et al., 2005; Wright et al., 2006; Geyer and Martí, 2008). Alternatively, crater-like bases could form by collapse of subsurface conduits following magma extraction and subsidence of overlying material (e.g. Walker, 1993; Geyer and Martí, 2008) and/or post-emplacement gravitational subsidence in response to volcano loading (e.g. Moore and Clague, 1992; de Silva and Lindsay, 2015); depressions generated by these subsidence processes are expected to host inward-dipping layers (e.g. de Silva and Lindsay, 2015). We consider it unlikely that the crater-like bases documented here (e.g., Figs 4a-d) formed by subsidence because: (i) gravitational subsidence driven by volcano loading could not produce craters volumetrically larger than, and which occasionally extend beyond the footprint of, the overlying edifices (Moore and Clague, 1992; de Silva and Lindsay, 2015) (Fig. 7i; Table 1); (ii) volcano loading will cause underlying reflections to sag and will *not* produce craters that truncate and erode underlying strata (Figs. 4a-d); and (iii) the sub-horizontal reflections observed within the crater-like bases are inconsistent with collapse of pre-existing strata into evacuated magma conduits or deformation imposed by the volcano load (Figs. 4a-d).

By ruling out subsidence as a mechanism for driving crater formation, our observed truncation and erosion of underlying strata by the craters may suggest they formed via an initial phase of explosive activity (e.g. Planke et al., 2005; Wright et al., 2006; Geyer and Martí, 2008). However, whilst evidence for explosive volcanism (e.g. pyroclast occurrence) has been documented in silicic, volatile-rich deep-water settings, high hydrostatic pressures caused by large water columns (e.g. >1.0 km) are expected to prevent exsolution of volatiles from magma and thereby inhibit explosive eruptions (e.g. Walker, 1993; de Silva and Lindsay, 2015; Carey et al., 2018; Cas and Simmons, 2018). Although we lack the well data required to test whether the crater-infilling-material was generated by explosive volcanic activity, we consider it plausible that the deep-water emplacement (>1.5 km) and the basaltic, inferred volatile-poor nature of magma extruded from these volcanoes may have restricted a namely "explosive" eruption style. In particular, the interplay of the deep-water setting and magma composition may have led to primarily effusive eruptions or magma extrusion into the water column in a "non-explosive" manner, e.g. such as suggested for high mass eruption rates by Manga et al. (2018). If explosive activity were inhibited, a different mechanism for producing the observed erosive craters is required.

Given the sub-horizontal seismic reflections (i.e. SF1) infilling the craters and truncation of underlying strata by the basal surface, we suggest the crater-like bases could have formed in response to the escape of magma-related hydrothermal fluids (e.g. fluids from magma and/or heated pore fluids from the surrounding sediments). We propose that fluid escape disaggregated and excavated the weak, near-seabed sediments via a similar process to that inferred for ancient, seismically-imaged hydrothermal vents (e.g. Planke et al., 2005; Buarque et al., 2016). Considering expelled, fine-grained sediments are likely to be removed by bottom currents (e.g. Judd and Hovland, 2007), we suggest the crater may have been infilled by sub-horizontal packages composed of either: (i) erupted dense material that settles out of the water column (i.e. it is not affected by bottom currents), perhaps forming layers of hyaloclastites; and/or (ii) material eroded from the depression flanks and deposited within the crater. The process we infer for the formation of the crater-like bases is similar to the generation of deep-water pockmarks, which are usually of kilometer-scale and infilled by sub-horizontal sedimentary strata (e.g. Judd and Hovland, 2007). Further exploration of the material filling these basin-like structures by drilling and coring would help clarify the style and nature of the eruptive activity and crater formation.

Regardless of the process(es) driving crater formation, the absence of crater-like bases beneath GP2 edifices indicates volcanism did not always involve near-seabed excavation and was site specific (Figs. 4e-f). It is difficult to determine exactly what factors (e.g. seabed cohesivity and porosity, water depth, mass eruption rate, magma composition and volatile content) controlled the initial emplacement styles of the GP1 and GP2 volcanoes solely from the geophysical data we use here.

5.2.2. Model of volcano growth

Volcano geometry is influenced by the interplay of constructive (e.g. dyke intrusion and stacking of lava flows) and destructive processes (e.g. flank collapse and erosion) (e.g. Annen et al., 2001; Kervyn et al., 2009; Magee et al., 2013). To evaluate edifice growth, field- and remote sensing-based studies broadly rely on the assumption that, in any given volcanic field or setting, small volcanoes develop into large volcanoes (e.g. Walker, 1993; de Silva and Lindsay, 2015). Patterns in volcano morphometry have therefore been used to infer growth models (e.g. Rossi, 1996; Calvès et al., 2011; Magee et al., 2013; Karlstrom et al., 2018). From these morphometric data, the following growth models for various volcanoes have been proposed (Fig. 8): (i) proportional increase in summit height and basal diameter, maintaining flank dip (Magee et al., 2013; Figs 8a, e); (ii) preferential addition of material to the summit area and upper volcano flanks, whilst the diameter remains consistent and flank dip increases with time (Magee et al., 2013; Figs 8b, e); (iii) lateral progradation of the edifice flanks while summit height is fixed, such that flank dip decreases with time (Calvès et al., 2011; Figs 8c, e); and (iv) maintenance of a proportional increase in summit height and basal diameter with time, interrupted by a short-stage of lateral progradation of the edifice flanks (Rossi, 1996; Figs 8d, e). However, these growth models derived from volcano morphometry data are difficult to test because we cannot easily access and evaluate the internal 3D structure of volcanoes. Seismic reflection data uniquely allows us to image volcano interiors in 3D, meaning we can interrogate how edifices build up through time by mapping internal layers (Magee et al. 2013; Sun et al., 2019).

The internal seismic facies variations of GP1 volcanoes differs from the seismic facies observed within monogenetic volcanoes that are mainly characterized by homogeneous seismic reflections (e.g. Reynolds et al., 2018). These facies differences suggest the GP1 volcanoes were instead formed through multiple eruptive events (i.e. they are polygenetic) and we propose they likely developed in three stages (Fig. 9): (Stage 1) during the first stage, crater-like bases formed through the explosive expulsion of hydrothermal fluids (see Section 5.2.1); (Stage 2) crater infilling through eruption of material and/or mass wasting of crater flanks, forming the aggradational SF1 facies; (Stage 3) construction of a broadly conical edifice on a relatively flat surface, following crater infilling, through summit eruptions that promoted vertical and lateral growth as evidenced by the positive correlation between volcano height and basal diameter, and the parallelism between their external morphology and internal SF2 reflections (cf. Figs. 4, 6a, 8a, e). Down-dip convergence of internal SF2 reflections in some volcanoes (e.g. V12; Fig. 4b) suggests that, for some edifices, vertical aggradation through accumulation of erupted material at the summit may have outpaced lateral expansion of the basal diameter (e.g. Figs. 8b, e) (Vail et al. 1977; Magee et al. 2013); i.e. in this scenario, little erupted material reached the base flanks of the volcano, perhaps because eruption rate was low and episodic. The growth of some volcanoes by vertical aggradation may explain why flank dips of the GP1 population correlate moderately positively with volcano height, but not basal diameter (Figs. 6b-c). During Stage 2 or Stage 3, after full or partial infilling of the crater-like base, intrusions feeding summit eruptions may have modified the core of SF1 to form the conical structures that are locally observed (Figs. 4a-d, 9).

GP2 volcanoes lack crater-like bases but otherwise appear similar to GP1 (Figs 4 and 6); i.e. the volcanic materials contained in the GP2 volcanoes were expelled directly onto the paleo-seabed, feeding a volcano that grew both vertically and laterally (Stage 3; Fig. 9). The narrow, low-amplitude zone directly beneath the volcanoes and associated deformations (e.g. deflected-upward seismic reflections) suggest that dykes or faults may have served as magma ascent pathways (MP) (Fig. 5). However, these upward-deflected seismic reflections may also be possibly interpreted as seismic artefacts (i.e. velocity pull-ups) that are caused by the overlying thick, high-density volcanic rocks.

5.2.3 Controls on edifice morphology

Compared to subaerial and shallow-water basaltic volcanoes, as well as moderate- to deep-water (0.9-3 km) andesitic-basaltic volcanoes, the deep-water basaltic volcanoes we study: (i) are ~41–427 times (in volumes) smaller than basal and basaltic-andesitic volcanoes from elsewhere

(Fig. 6a, d-e; Table S1); (ii) display similar positive correlations between height, diameter, and volume, implying volcano growth broadly involved a proportionate increase in summit height and basal diameter (Fig. 8-9) (e.g., Magee et al., 2013); but (iii) have steeper flanks (most of them >20°), with some volcanoes evidently growing via preferential vertical aggradation (Fig. 6b-c). We tentatively suggest that the small size and steeper flanks we observe likely reflect differences in the environment of emplacement (e.g., water depth) and seabed lithology. Below we consider how mass eruption rate and magma volatile content may control the geomorphological characteristics of volcanoes in this study.

The magnitude, duration, and steadiness of eruption rate influence the distribution of extruded material (e.g. de Silva and Lindsay, 2015; White et al., 2015). For example, low eruption rates drive lava to move slowly over short distances (e.g. Rossi, 1996) and, thus, erupted materials are more likely to accumulate around the vents/upper flanks and form high-angle slopes; i.e. growth is via preferential vertical aggradation. Low eruption rates could explain the steep slopes of the volcanoes we study, and may relate to the limited magma supply during post-rift volcanism (e.g. Yan et al., 2006; Li et al., 2014) and/or volatile undersaturation in the basaltic parental magma. Episodic, shorter-duration emplacement of lava (as opposed to a single event) would also build notably steeper flanked volcanoes, as demonstrated in experiments by Fink et al. (1993). However, we note that the presence of long run-out lava flows flanking the volcano edifices (>9.0 km long) likely indicates eruption rates varied significantly through time, with intermittent periods of short-lived, high eruption rates of, possibly, volatile-enriched magma feeding the longest run-out flows (Sun et al., 2019) (Fig. 5). In addition to the low mass eruption rates, volatile-undersaturated lavas (as inferred here) have higher cooling rates and higher glass transition temperatures and higher viscosities, and thus, lava may quench and build-up more proximal to the eruptive source (Del Gaudio et al., 2007).

Because of high hydrostatic pressure, wet, cold, and unconsolidated sediments, and the overall magma-deficient (low eruption rate and magma supply), post-rift setting during the Late Miocene, the deep-water volcanoes documented here geomorphologically and genetically differ to their subaerial and shallow-water counterparts in other tectonic environments (Fig. 6). In future, physical and geochemical studies of eruptive products, particularly within GP1 volcanoes, may help resolve the unusual morphologies and eruptive mechanisms within this tectonic setting.

6. Conclusion

We use 3D seismic reflection data to investigate the three-dimensional structure of thirteen Late Miocene-to-Quaternary deep-water volcanoes. Two groups of volcanoes, one with (GP1) and one without (GP2) crater-like bases, are identified. Internally, these volcanoes comprise two dominant seismic facies types that document volcano growth processes. We are able to investigate the relationship between the external morphology and internal structure of deep-water volcanoes, and thereby build growth models for these hitherto poorly understood volcanic structures. The growth of most of the volcanoes is defined by two main stages: crater formation and infilling, likely initiated by the escape of hydrothermal fluids, and subsequent construction of an overlying conical edifice. Importantly, recognition of crater-like bases beneath the volcanoes implies the volume of modern deep-water volcanoes, which are typically quantified by bathymetric surveys, may be grossly underestimated as the volcanoes may not have a flat, seabed-parallel base. In this study, most of the deep-water volcanoes have edifice volumes less than the underlying craters.

Our growth models suggest the morphology of the studied deep-water volcanoes were primarily controlled by the high hydrostatic pressure occurring in the deep-water setting, the volatile-poor nature of the parent magma, and variable magma supply due to the post-rift tectonic setting. In particular, these factors led to erupted material primarily accumulating near the summit and on the upper flanks of the volcanoes, meaning they have relatively smaller sizes (basal diameters, heights and volumes) and are characterized by slopes steeper than that typically seen in their subaerial, shallow-water, and deep-water arc-related counterparts. This study adds a unique dataset to the global database of submarine volcano morphologies. Moreover, this study also highlights that 3D seismic surveys could help to revise previous estimates of submarine volcano or seamount volumes and morphologies, and to further our understanding of submarine volcanoes that are already relatively-well studied.

Acknowledgment

This work was supported by the National Scientific Foundation of China (Grant Nos. 41676051 and 41372112), the Programme of Introducing Talents of Discipline to Universities (No. B14031) and the China Scholarship Council (201906415013). We thank the China National Offshore Oil Company for permission to release the data. The reflection seismic data may be requested from this Company (https://www.cnoocltd.com/). Editor Jean-Philippe Avouac, and journal reviewers Deniz Cukur and two anonymous reviewers are thanked for their invaluable comments and suggestions.

References

Annen, C., Lénat, J.F., Provost, A., 2001. The long-term growth of volcanic edifices: numerical modelling of the role of dyke intrusion and lava flow emplacement. J. Volcanol. Geotherm. Res. 105, 263-289, https://doi.org/10.1016/S0377-0273(00)00257-2.

Arnulf, A.F., Harding, A.J., Kent, G.M., Carbotte, S.M., Canales, J.P., Nedimović, M.R., 2014. Anatomy of an active submarine volcano. Geology, 42, 655-658, https://doi.org/10.1016/10.1130/G35629.1.

Briais, A., Patriat, P., Tapponnier, P., 1993. Updated interpretation of magnetic anomalies and seafloor spreading stages in the South China Sea: Implications for the Tertiary tectonics of Southeast Asia. J. Geophys. Res. 98, 6299-6328, https://doi.org/10.1029/92JB02280.

Brown, A. R., 2004. Interpretation of three-dimensional seismic data: AAPG Memoir 42, 6thed. SEG Investigations in Geophysics.

Buarque, B.V., Barbosa, J.A., Magalhães, J.R.G., Oliveira, J.T.C., Filho, O.J.C., 2016. Post-rift volcanic structures of the Pernambuco Plateau, northeastern Brazil. J. S. Am. Earth, Sci. 70, 251-267, http://dx.doi.org/10.1016/j.jsames.2016.05.014.

Buchs, D.M., Williams, R., Sano, S., Wright, V.P., 2018. Non-Hawaiian lithostratigraphy of Louisville seamounts and the formation of high-latitude oceanic islands and guyots. J. Volcanol. Geotherm. Res. 356, 1-23, https://doi.org/10.1016/j.jvolgeores.2017.12.019.

Calvès, G., Schwab, A.M., Huuse, M., Clift, P.D., Gaina, C., Jolley, D., Tabrez, A.R., Inam, A., 2011. Seismic volcanostratigraphy of the western Indian rifted margin: The pre-Deccan igneous province. J. Geophys. Res. 116, B01101, https://doi.org/10.1029/2010JB000862.

Carey, R., Soule, S.A., Manga, M., White, J.D.L., McPhie, J., Wysoczanski, R., Jutzeler, M., Tani, K., Yoerger, D., Fornari, D., Caratori-Tontini, F., Houghton, B., Mitchell, S., Ikegami, F., Conway, C., Murch, A., Fauria, K., Jones, M., Cahalan, R., and McKenzie, W., 2018. The largest deep-ocean silicic volcanic eruption of the past century. Sci. Adv. 4, e1701121, https://doi.org/10.1126/sciadv.1701121.

Cas, R.A.F., Simmons, J., 2018. Why deep-water eruptions are so different from subaerial eruptions? Front. Earth Sci. 6, https://doi.org/10.3389/feart.2018.00198.

Clague, D.A., Paduan, J.B., Dreyer, M.B., Chadwick Jr, D.M., Rubin, K.R., Perfit, M.R., Fundis, A.T., 2018. Chemical Variations in the 1998, 2011, and 2015 Lava Flows From Axial Seamount, Juan de Fuca Ridge: Cooling During Ascent, Lateral Transport, and Flow. Geochem. Geophys. Geosyst. 19, 2915-2933, https://doi.org/10.1029/2018GC007708.

Clift, P.D., Lin, J., and ODP Leg 184 Scientific Party, 2001. Patterns of extension and magmatism along the continent-ocean boundary, South China margin. Geological Society, London, Special Publications, 187, 489-510, https://doi.org/10.1144/GSL.SP.2001.187.01.24.

Cullen, A., Reemst, P., Henstra, G., Gozzard, S., Ray, A., 2010. Rifting of the South China Sea: new perspectives. Petrol. Geosci. 16, 273-282, https://doi.org/10.1144/1354-079309-908.

Del Gaudio, P., Behrens, H., Deubener, J., 2007. Viscosity and glass transition temperature of hydrous float glass. J. Non-cryst. Solids. 353, 223-236, https://doi.org/10.1016/j.jnoncrysol.2006.11.009.

de Silva, S., Lindsay, J.M., 2015, Primary volcanic landforms. In: Sigurdsson, H., Houghton, B.F., McNutt, S.R., Rymer, H., Stix, J. (eds), Encyclopedia of volcanoes, 2nd ed. Academic, London, pp 273-297, http://dx.doi.org/10.1016/B978-0-12-385938-9.00015-8.

Eide, C.H., Schofield, N., Jerram, D.A., Howell, J., 2017. Basin-scale architecture of deeply emplaced sill complexes: Jameson Land, East Greenland. J. Geol. Soc. London. 174, 23-40, https://doi.org/10.1144/jgs2016-018.

Fink, J.H., Bridges, N.T., Grimm, R.E., 1993. Shapes of Venusian “pancake” domes imply episodic emplacement and silicic composition. Geophys. Res. Lett. 20,261-264, https://doi.org/10.1029/92GL03010.

Franke, D., Savva,D., Pubellier, M., Steuer, S., Mouly, B., Auxietre, J., Meresse, F., Chamot-Rooke, N., 2014. The final rifting evolution in the South China Sea. Mar. Petrol. Geol. 58, 704-720, https://doi.org/10.1016/j.marpetgeo.2013.11.020.

Geyer, A., Martí, J., 2008. The new worldwide collapse caldera database (CCDB): a tool for studying and understanding caldera processes. J. Volcanol. Geotherm. Res. 175, 334-354, http://dx.doi.org/10.1016/j.jvolgeores.2008.03.017.

Goto, Y., Tomiya, A., 2019. Internal Structures and Growth Style of a Quaternary Subaerial Rhyodacite Cryptodome at Ogariyama, Usu Volcano, Hokkaido, Japan. Front. Earth Sci. 7, 66, https://doi.org/10.3389/feart.2019.00066.

Gregg, T.K.P., Fornari, D.J., 1998. Long submraine lava flows: Observations and results from numerical modeling. J. Geophys. Res. 103, 27517-27531, https://doi.org/10.1029/98JB02465.

Grosse, P., van Wyk de Vries, B., Petrinovic, I.A., Euillades, P.A., Alvarado, G.E., 2009. Morphometry and evolution of arc volcanoes. Geol. Soc. Am. 37, 651-654, https://doi.org/10.1130/G25734A.1.

Jackson, C.A.-L., 2012. Seismic reflection imaging and controls on the preservation of ancient sill-fed magmatic vents. J. Geol. Soc. London 169, 503-506, https://doi.org/10.1144/0016-76492011-147.

Judd, A.G., and Hovland, M., 2007, Seabed Fluid Flow: The Impact on Geology, Biology and the Marine Environment. Cambridge University Press, Cambridge, pp. 163-178.

Karlstrom, L., Richardson, P.W., O'Hara, D., Ebmeier, S.K., 2018. Magmatic Landscape Construction. J. Geophys. Res.- EARTH, 123, 1710-1730, https://doi.org/10.1029/2017JF004369.

Kervyn, M., Ernst, G.G.J., van Wyk de Vries, B., Mathieu, L., Jacobs, P., 2009. Volcano load control on dyke propagation and vent distribution: Insights from analogue modelling. J. Geophys. Res. 114, B03401, https://doi.org/10.1029/2008JB005653.

Larsen, H.C., Mohn, G., Nirrengarten, M., Sun, Z., Stock, J., Jian, Z., Klaus, A., Alvarez-Zarikian, C.A., Boaga, J., Bowden, S.A., Briais, A., Chen, Y., Cukur, D., Dadd, K., Ding, W., Dorais, M., Ferré, E.C., Ferreira, F., Furusawa, A., Gewecke, A., Hinojosa, J., Höfig, T.W., Hsiung, K.H., Huang, B., Huang, E., Huang, X.L., Jiang, S., Jin, H., Johnson, B.G., Kurzawski, R.M., Lei, C., Li, B., Li, L., Li, Y., Lin, J., Liu, C., Liu, C., Liu, Z., Luna, A.J., Lupi, C., McCarthy, A., Ningthoujam, L., Osono, N., Peate, D.W., Persaud, P., Qiu, N., Robinson, C., Satolli, C., Sauermilch, I., Schindlbeck, J.C., Skinner, S., Straub, S., Su, X., Su, C., Tian, L., van der Zwan, F.M., Wan, S., Wu, H., Xiang, R., Yadav, R., Yi, L., Yu, P.S., Zhang, C., Zhang, J., Zhang, Y., Zhao, N., Zhong, G., Zhong, L., 2018. Rapid transition from continental breakup to igneous oceanic crust in the South China Sea. Nat. Geosci. 11, 782-789, https://doi.org/10.1038/s41561-018-0198-1.

Lester, R., Van Avendonk, H.J.A., McIntosh, K., Lavier, L., Liu, C.S., Wang, T.K., Wu, F., 2014. Rifting and magmatism in the northeastern South China Sea from wide-angle tomography and seismic reflection imaging. J Geophys. Res. 119, 2305-2323, https://doi.org/10.1002/2013JB010639.

Li, P., and Liang, H., 1994. Cenozoic magmatism in the Pearl River Mouth Basin and its relationship to the basin evolution and petroleum accumulation. Guangdong Geology, 9, 23-34.

Li, C.F., Xu, X., Lin, J., Sun, Z., et al., 2014. Ages and magnetic structures of the South China Sea constrained by the deep tow magnetic surveys and IODP Expedition 349. Geochem. Geophys. Geosyst. 15, 4958-4983, https://doi.org/10.1002/2014GC005567.

Lüdmann, T., Wong, H., 1999. Neotectonic regime on the passive continental margin of the northern South China Sea. Tectonophysics 311, 113-138, https://doi.org/10.1016/S0040-1951(99)00155-9.

Magee, C., Hunt-Stewart, E., Jackson, C.A.-L., 2013. Volcano growth mechanisms and the role of sub-volcanic intrusions: Insights from 2D seismic reflection data. Earth Planet. Sci. Lett. 373, 41-53, https://doi.org/10.1016/j.epsl.2013.04.041.

Manga, M., Fauria, K.E., Lin, C., Mitchell, S.J., Jones, M., Conway, C.E., Degruyter, W., Hosseini, B., Carey, R., Cahalan, R., Houghton, B.F., White, J.D.L., Jutzeler, M., Soule, S.A., Tani, K., 2018. The pumice raft-forming 2012 Havre submarine eruption was effusive. Earth Planet. Sci. Lett. 489, 49-58, https://doi.org/10.1016/j.epsl.2018.02.025.

Moore, J.G., Clague, D.A., 1992. Volcano growth and evolution of the island of Hawaii. Geol. Soc. Am. Bull. 104, 1471-1484, https://doi.org/10.1130/0016-7606(1992)104<1471:VGAEOT>2.3.CO;2.

Planke, S., Rasmussen, T., Rey, S.S., Myklebust, R., 2005. Seismic characteristics and distribution of volcanic intrusions and hydrothermal vent complexes in the Vøring and Møre Basins. In: Dore, A.G., Vining, B. (Eds.), Proceedings of the 6th Petroleum Geology Conference on Petroleum Geology: N.W. Europe and Global Perspectives, pp. 833-844.

Reynolds, P., Schofield, N., Brown, R.J. Holford, S.P., 2018. The architecture of submarine monogenetic volcanoes-insights from 3D seismic data. Bas. Res. 30, 437-451, https://doi.org/10.1111/bre.12230.

Rossi, M.J., 1996. Morphology and mechanism of eruption of post glacial shield volcanoes in Iceland. Bull. Volcanol. 57, 530-540, https://doi.org/10.1007/BF00304437.

Smith, D.K., 1988. Shape analysis of Pacific seamounts. Earth Planet. Sci. Lett. 90, 457-466.

Staudigel, H., Clague, D.A., 2010. The geological history of deep-sea volcanoes: biosphere, hydrosphere, and lithosphere interactions. Oceanography, 23, 58-71, https://doi.org/10.5670/oceanog.2010.62.

Sun, Q.L., Jackson, C.A-L., Magee, C., Mitchell, S.J., Xie, X.N., 2019. Extrusion dynamics of deep-water volcanoes. Solid Earth Discuss., https://doi.org/10.5194/se-2019-87.

Vail, P.R., Todd, R.G., Sangree, J.B., 1977. Seismic stratigraphy and global changes in sea level, part 5. In: Payton, C.E. (Ed.), Seismic Stratigraphy: Application to Hydrocarbon Exploration, 8th edition. American Association of Petroleum Geologists, pp. 99-116.

Walker, G.P.L., 1993. Basaltic-volcano systems. In: Magmatic Processes and Plate Tectonics, edited by Pritchard, H.M., Alabaster, T., Harris, N.B.W., Neary, C.R., Geological Society Special Publication, 76: 3-38.

Wright, I.C., Worthington, T.J., Gamble, J.A., 2006. New multibeam mapping and geochemistry of the 30°–35° S sector, and overview, of southern Kermadec arc volcanism. J. Volcanol. Geotherm. Res., 149, 263-296, https://doi.org/10.1016/j.jvolgeores.2005.03.021.

Wei, X.D., Ruan, A.G., Zhao, M.H., Qiu, X.L., Li, J.B., Zhu, J.J., Wu, Z.L., and Ding, W.W., 2011. A wide-angle OBS profile across the Dongsha uplift and Chaoshan depression in the mid-northern South China Sea. Chinese Journal of Geophysics, 54, 3325-3335, https://doi.org/10.3969/j.issn.0001-5733.2011.12.030.

White, J.D.L., McPhie, J., Soule, S.A., 2015. Submarine lavas and hyaloclastite. In: Sigurdsson, H., Houghton, B.F., McNutt, S.R., Rymer, H., Stix, J. (eds), Encyclopedia of volcanoes, 2nd edn. Academic, London, pp 363–375, http://dx.doi.org/10.1016/B978-0-12-385938-9.00019-5.

Xu, S.C., Yang, S.K., Huang, L.F., 1995. The application of sequence stratigraphy to stratigraphic correlation. Earth Science Frontiers, 2, 115-123.

Yan, P., Deng, H., Liu, H.L., Zhang, Z., Jiang, Y., 2006. The temporal and spatial distribution of volcanism in the South China Sea region. J. Asian Earth Sci. 27, 647-659, https://doi.org/10.1016/j.jseaes.2005.06.005.

Yan, P., Zhou, D., and Liu, Z.S., 2001. A crustal structure profile across the northern continental margin of the South China Sea. Tectonophysics, 338, 1-21, https://doi.org/10.1016/S0040-1951(01)00062-2.

Yang, S., Qiu, Y., and Zhu, B., 2015, Atlas of Geology and Geophysics of the South China Sea: China Navigation Publications, Tianjin.

Zhao, F., Alves, T.M., Wu, S.G., Li, W., Huuse, M., Mi, L.J., Sun, Q.L., Ma, B.J., 2016. Prolonged post-rift magmatism on highly extended crust of divergent continental margins (Baiyun Sag, South China Sea). Earth Planet. Sci. Lett. 445, 79-91, https://doi.org/10.1016/j.epsl.2016.04.001.

Zou, H.P., Li, P.L., Rao, C.T., 1995. Geochemistry of Cenozoic volcanic rocks in Zhujiangkou basin and its geodynamic significance. Geochemica, 24, 33-45.

Figure Captions

Figure 1: (a) Geological setting of the study area. Red polygonal line located to the south of Dongsha Islands is the 3D seismic survey. Top left: regional setting of the South China Sea. It is bounded by the Red River Strike-slip faults (RRFs) to the west and by the subduction trench (Manila Trench) to the east. Northern South China Sea is marked with black square. Igneous rocks with ages from exploration wells and seamount dredges are marked with blue circles/rings (Jin, 1989; Li and Liang, 1994; Zou et al., 1995). Crustal structure profiles (OBS1993 (Yan et al., 2001) and OBS2006-3 (Wei et al., 2011)) are marked with pink solid lines. ODP sites 1145 and1146, IODP site U1501 and location of Figure 3 are also labeled. The base map is modified from Yang et al. (2015) and Sun et al. (2019); (b) and (c) Regional seismic strata of the study area. Volcanic materials are mainly located in the shallow level (0-300 m) of post-rifting strata. See location in (a).

Figure 2: (a) Schematic diagram of the calculation method for igneous velocity within the volcano and surrounding sediments; (b) Schematic diagram of geomorphic parameters measured in this study, using an example volcano with an identified crater-like base and overlying edifice. Note that the travel-time distances between the volcano summit and its base (Ts), or the top of the

velocity pull-up (Ti), were measured *within* the volcano edifices.

Figure 3: (a) Present seabed morphologies of the study area, interpreted from the 3D seismic data. The landmark areal projections of buried or partly buried volcanoes are marked; (b) Thickness (and thus, height) of volcano edifices in the study area; (c) Thickness (and thus, depth) of volcano craters in the study area; (d) Total thickness of the volcanoes, calculated from the vertical addition of (b) and (c). The boundaries of merged volcanoes are marked. 100 ms (twt) = ~200 m.

Figure 4: (a) - (d): Seismic characteristics of volcanoes (GP1). (a) Volcano 9 (V9) and its line drawing; (b) Volcano 12 (V12) and its line drawing; (c) Volcano 1 (V1) and its line drawing; (d) Volcano 7 (V7) and its line drawing. (e) - (f): Seismic characteristics of volcanoes (GP2). (e) Volcano 8 (V8) and its line drawing; (f) Volcano 6 (V6) and its line drawing. 150 ms (twt) for volcano is equal to ~300 m. TV = top of volcano; PS = present seabed (solid pink line); PLS = paleo-seabed (solid green line); IS = inferred present seabed (dashed pink line); SF1 = seismic facies 1; SF2 = seismic facies 2; VE. = vertical exaggeration. See locations in Fig. 3a.

Figure 5: 3D seismic profile crosses through V8, V9 and V10. The igneous pathways underneath the volcanoes are narrow, vertical structures (dashed arrows) and the surrounding strata are slightly pushed upward, suggesting them probably as dykes. VE. = vertical exaggeration. See location in Fig. 3a.

Figure 6: Geomorphologic parameters of deep-water volcanoes (gray solid circles; this study),

shallow-water volcanoes (pink squares; Magee et al., 2013), subaerial arc volcanoes (green triangles; Grosse et al., 2009), submarine arc volcanoes (grey cross; Wright et al., 2006) and ocean volcanoes (blue rhombus; Smith, 1988). (a) Height vs diameter; (b) Dip vs diameter; (c) Dip vs height; (d) Diameter vs volume; (e) Height vs volume; (f) Dip vs volume; The deep-water volcanoes in this study have different trends (slopes) to other types. The errors of geomorphologic parameters of volcanoes in the study area are from the ranges of volcano velocities.

Figure 7: (a)-(f): Geomorphologic characteristics of the craters of deep-water volcanoes in this study. (a) Depth vs diameter (crater); (b) Dip vs diameter (crater); (c) Dip (crater) vs depth; (d) Depth vs volume (crater); (e) Diameter (crater) vs volume (crater); (f) Dip (crater) vs volume (crater). (g)-(i): Geomorphologic characteristics between the volcano edifices and craters of deep-water volcanoes. (g) Height vs depth; (h) Diameter (crater) vs diameter (edifice); (i) Volume (crater) vs volume (edifice); (j)-(l): Geomorphologic characteristics of the total volcanoes. (j) (Height + depth) vs average diameter; (k) (Height + depth) vs total volume; (l) Average diameter vs total volume.

Figure 8: Possible volcano growth models. (a) Model of shallow-water volcano growth (red dashed lines) through a proportional increase in summit height and basal diameter (offshore southern Australia; Magee et al., 2013); (b) Model of shallow-water volcano growth (green dashed lines) where summit height increases, whilst basal diameter remains consistent (offshore southern Australia; Magee et al., 2013); (c) Model of shallow-water and sub-aerial pioneer cones of hyaloclastite mounds (dark blue dashed lines) where the basal diameter increases, whilst the

summit height remains consistent (western Indian rifted margin; Calvès et al., 2011); (d) Model of sub-aerial shield volcano growth (orange dashed lines) involving a proportional increase in summit height and basal diameter, which is disrupted by a short stage of preferentially lateral progradation of the edifice flanks (Iceland, Rossi, 1996). (e) The expected trends in summit or basal diameter plotted against volcano volume and average flank dip for all models (a-d).

Figure 9: Cartoon showing proposed three-stage evolution of GP1 volcanoes (see text for details). GP2 volcano growth may be akin to Stage 3. SF1 = Seismic facies 1; SF2 = Seismic facies 2; MP = Possible magmatic intrusions.

Table Caption

Table 1: Geometrical parameters of the edifices and craters of volcanoes. (1) = water depth of the seabed where the volcanoes emplace or emplace underneath it (W.D.); (2) = sediment thickness overlying the buried volcanoes (Th.).

Figure 1

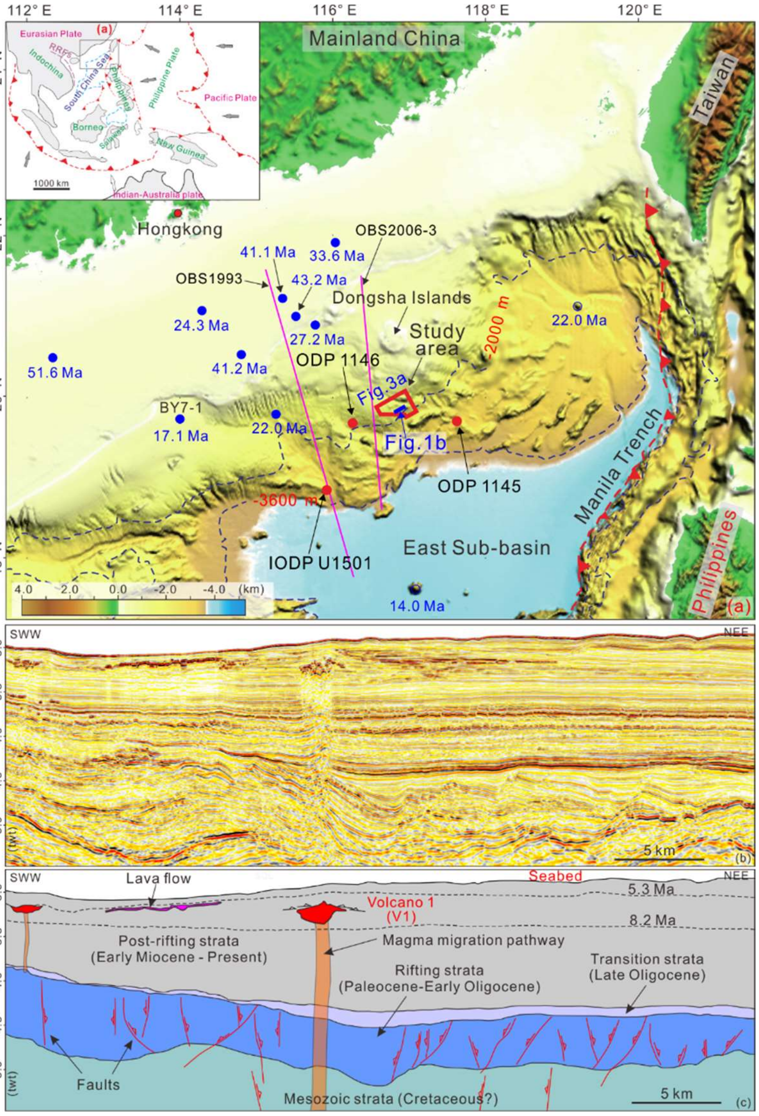
112° E
114° E
116° E
118° E
120° E
24° N
22° N
20° N
18° N
Mainland China
Taiwan
Hongkong
OBS2006-3
OBS1993
Dongsha Islands
Study area
2000 m
Fig.3a
Fig.1b
ODP 1146
ODP 1145
BY7-1
IODP U1501
-3600 m
East Sub-basin
Manila Trench
Philippines
51.6 Ma
24.3 Ma
41.1 Ma
33.6 Ma
43.2 Ma
27.2 Ma
41.2 Ma
17.1 Ma
22.0 Ma
22.0 Ma
14.0 Ma
4.0 2.0 0.0 -2.0 -4.0 (km)
(a)
Eurasian Plate
Indochina
South China Sea
Philippine Plate
Pacific Plate
Borneo
New Guinea
Indian-Australia plate
1000 km
SWW
NEE
5 km
(b)
Lava flow
Seabed
5.3 Ma
8.2 Ma
Volcano 1
(V1)
Magma migration pathway
Post-rifting strata
(Early Miocene - Present)
Rifting strata
(Paleocene-Early Oligocene)
Transition strata
(Late Oligocene)
Faults
Mesozoic strata (Cretaceous?)
(c)

Figure 2

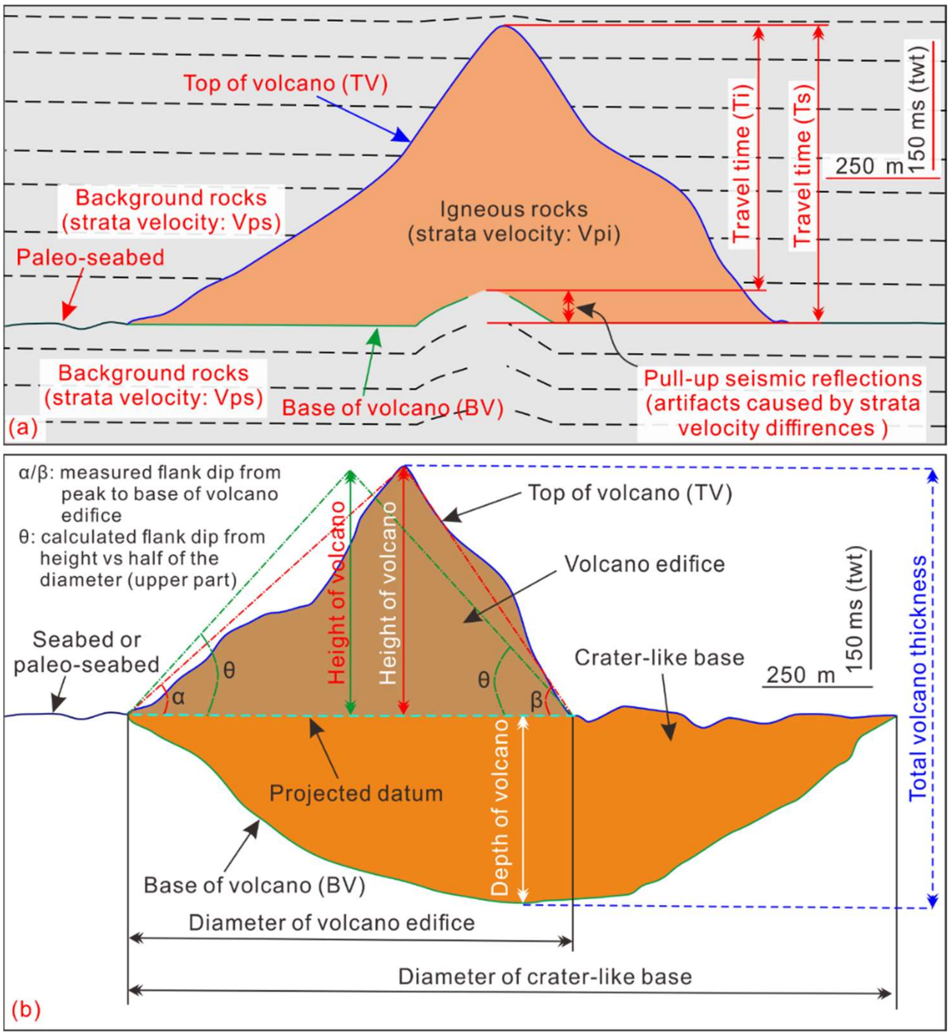

Top of volcano (TV)
Travel time (Ti)
Travel time (Ts)
150 ms (twt)
250 m
Background rocks
(strata velocity: Vps)
Igneous rocks
(strata velocity: Vpi)
Paleo-seabed
Background rocks
(strata velocity: Vps)
Base of volcano (BV)
Pull-up seismic reflections
(artifacts caused by strata
velocity diffirences)
(a)
α/β: measured flank dip from
peak to base of volcano
edifice
θ: calculated flank dip from
height vs half of the
diameter (upper part)
Top of volcano (TV)
Volcano edifice
Height of volcano
Height of volcano
150 ms (twt)
Total volcano thickness
Seabed or
paleo-seabed
θ
α
θ
β
Crater-like base
250 m
Projected datum
Depth of volcano
Base of volcano (BV)
Diameter of volcano edifice
Diameter of crater-like base
(b)

705 Figure 3

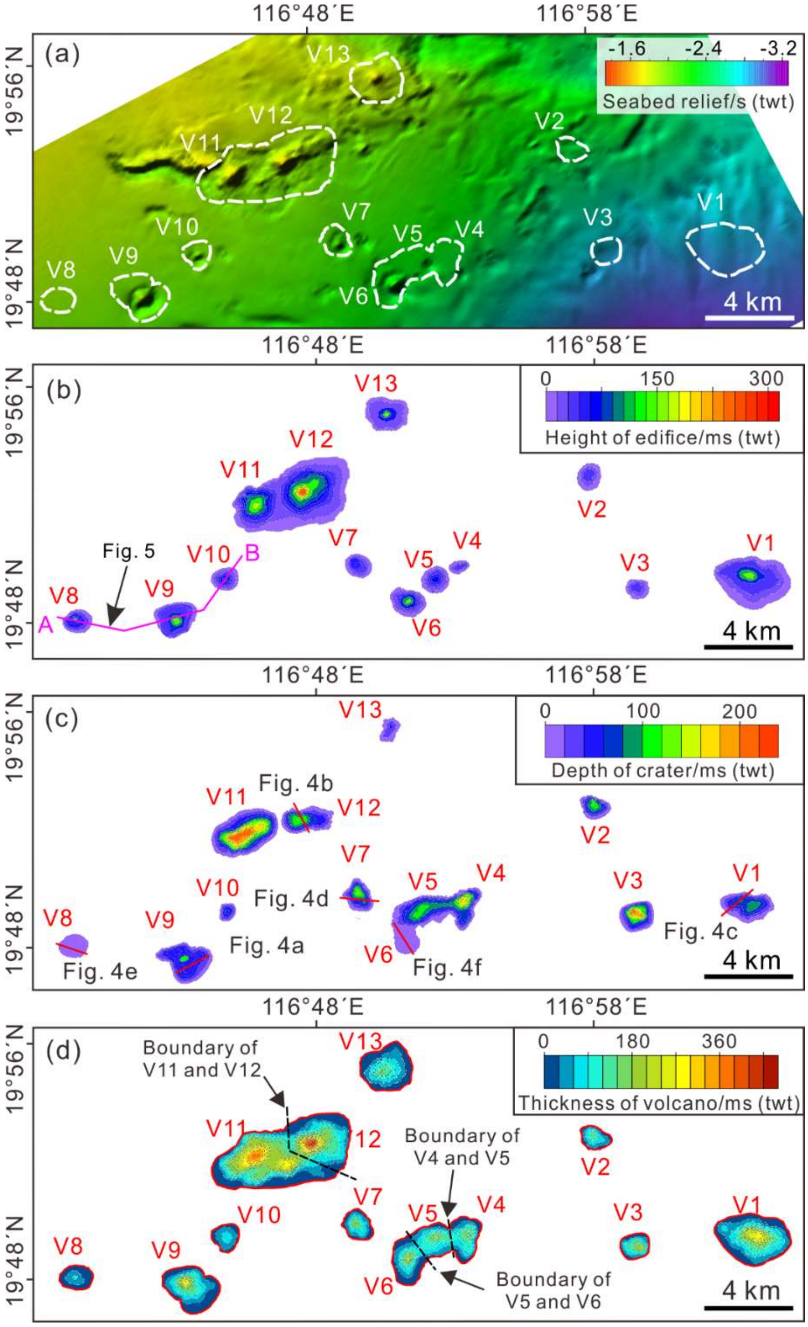

706

Figure 4

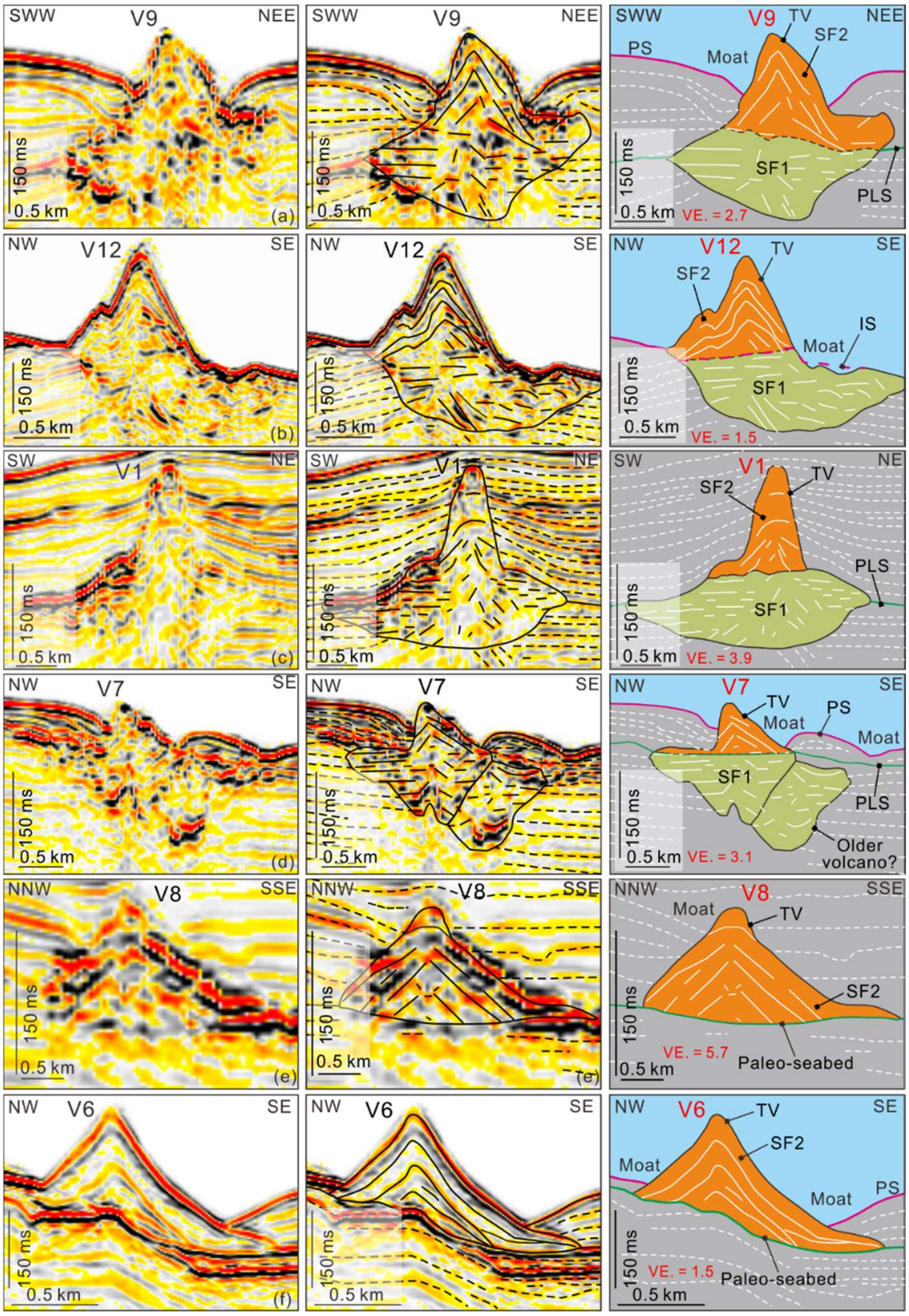

SWW
V9
NEE
150 ms
0.5 km
(a)
PS
TV
SF2
Moat
SF1
PLS
VE. = 2.7
NW
V12
SE
(b)
IS
VE. = 1.5
SW
V1
NE
(c)
VE. = 3.9
V7
(d)
Older volcano?
VE. = 3.1
NNW
V8
SSE
(e)
Paleo-seabed
VE. = 5.7
V6
(f)

Figure 5

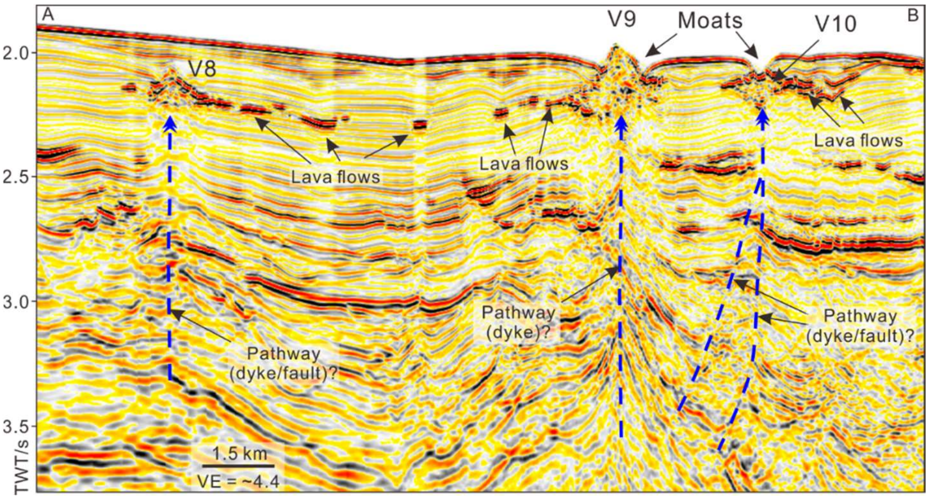
A
B
V8
V9
Moats
V10
Lava flows
Lava flows
Lava flows
Pathway (dyke/fault)?
Pathway (dyke)?
Pathway (dyke/fault)?
2.0
2.5
3.0
3.5
TWT/s
1.5 km
VE = ~4.4

Figure 6

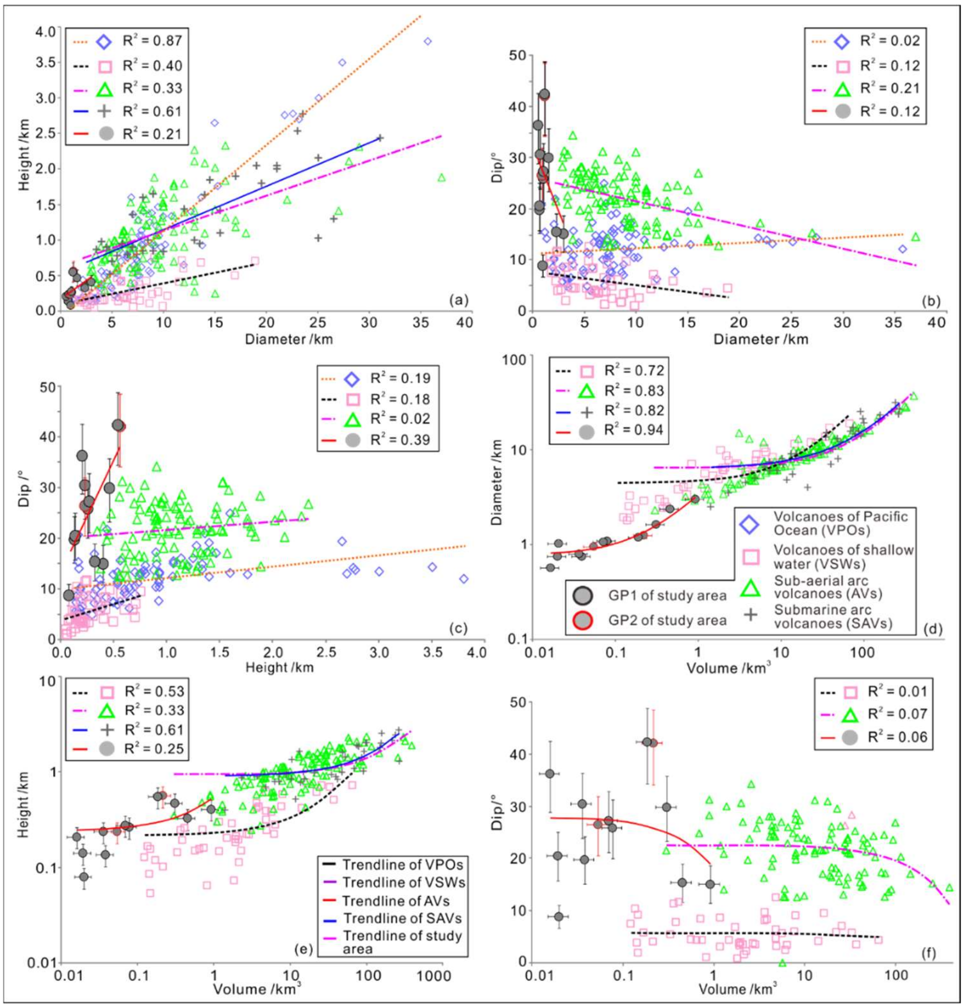

R² = 0.87
R² = 0.40
R² = 0.33
R² = 0.61
R² = 0.21
Height /km
Diameter /km
(a)
R² = 0.02
R² = 0.12
R² = 0.21
R² = 0.12
Dip /°
Diameter /km
(b)
R² = 0.19
R² = 0.18
R² = 0.02
R² = 0.39
Dip /°
Height /km
(c)
R² = 0.72
R² = 0.83
R² = 0.82
R² = 0.94
Diameter /km
Volume /km³
Volcanoes of Pacific Ocean (VPOs)
Volcanoes of shallow water (VSWs)
Sub-aerial arc volcanoes (AVs)
Submarine arc volcanoes (SAVs)
GP1 of study area
GP2 of study area
(d)
R² = 0.53
R² = 0.33
R² = 0.61
R² = 0.25
Height /km
Volume /km³
Trendline of VPOs
Trendline of VSWs
Trendline of AVs
Trendline of SAVs
Trendline of study area
(e)
R² = 0.01
R² = 0.07
R² = 0.06
Dip /°
Volume /km³
(f)

Figure 7

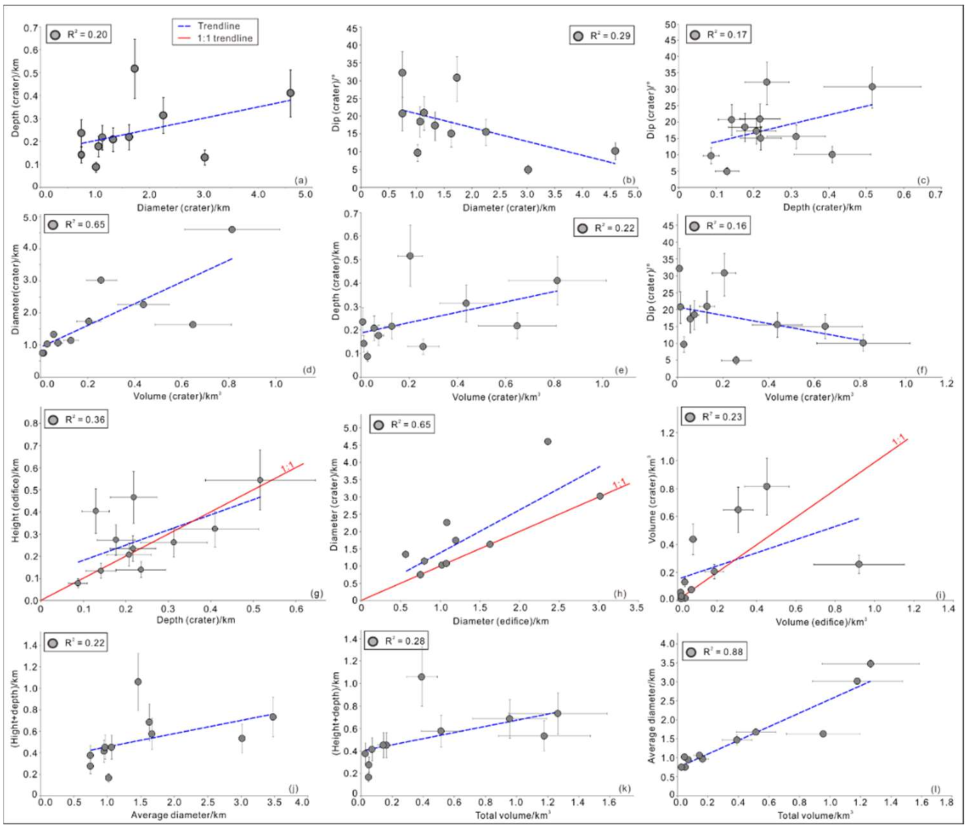

Trendline
1:1 trendline
R^2 = 0.20
Depth (crater)/km
Diameter (crater)/km
(a)
R^2 = 0.29
Dip (crater)/°
Diameter (crater)/km
(b)
R^2 = 0.17
Dip (crater)/°
Depth (crater)/km
(c)
R^2 = 0.65
Diameter(crater)/km
Volume (crater)/km³
(d)
R^2 = 0.22
Depth (crater)/km
Volume (crater)/km³
(e)
R^2 = 0.16
Dip (crater)/°
Volume (crater)/km³
(f)
R^2 = 0.36
Height (edifice)/km
Depth (crater)/km
1:1
(g)
R^2 = 0.65
Diameter (crater)/km
Diameter (edifice)/km
1:1
(h)
R^2 = 0.23
Volume (crater)/km³
Volume (edifice)/km³
1:1
(i)
R^2 = 0.22
(Hight+depth)/km
Average diameter/km
(j)
R^2 = 0.28
(Height+depth)/km
Total volume/km³
(k)
R^2 = 0.88
Average diameter/km
Total volume/km³
(l)

Figure 8

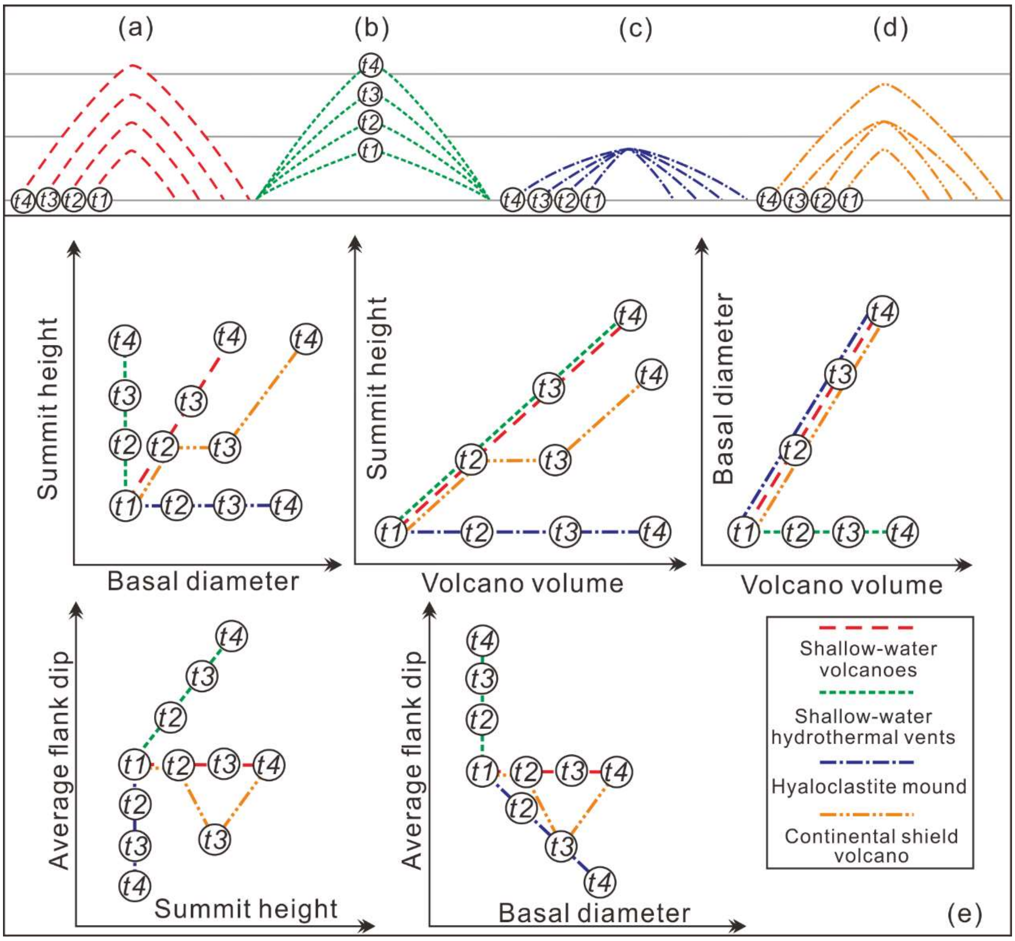

(a)
(b)
(c)
(d)
(e)
Summit height
Basal diameter
Volcano volume
Basal diameter
Volcano volume
Average flank dip
Summit height
Average flank dip
Basal diameter
Shallow-water volcanoes
Shallow-water hydrothermal vents
Hyaloclastite mound
Continental shield volcano

Figure 9

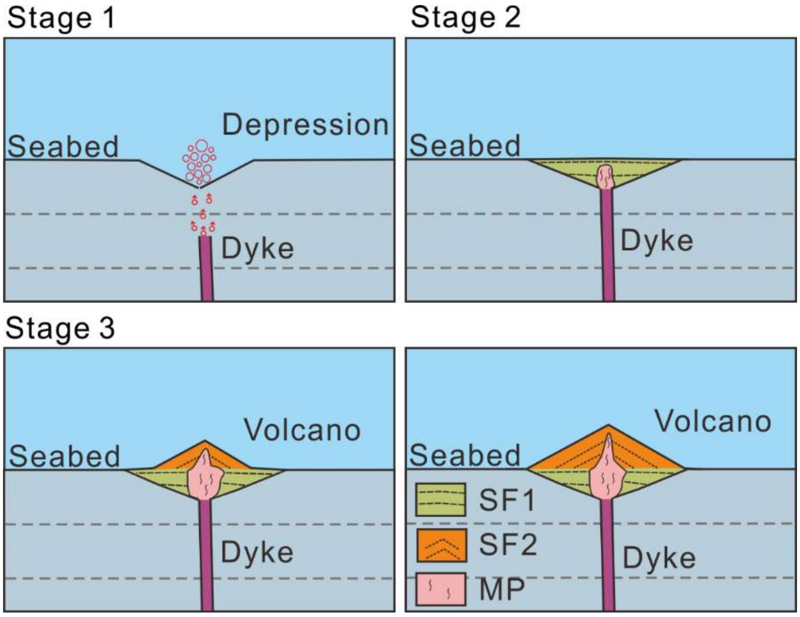

Stage 1
Seabed
Depression
Dyke
Stage 2
Seabed
Dyke
Stage 3
Seabed
Volcano
Dyke
Seabed
Volcano
SF1
SF2
MP
Dyke